https://doi.org/10.1016/j.cej.2021.131489

Unraveling Iron Speciation on Fe-biochar with Distinct Arsenic Removal Mechanisms and Depth Distributions of As and Fe

Zibo Xu [a], Zhonghao Wan [a], Yuqing Sun [a], Xinde Cao [b], Deyi Hou [c], Daniel S. Alessi [d], Yong Sik Ok [e], Daniel C.W. Tsang [a, *]

[a] Department of Civil and Environmental Engineering, The Hong Kong Polytechnic University, Hung Hom, Kowloon, Hong Kong, China.

[b] School of Environmental Science and Engineering, Shanghai Jiao Tong University, 800 Dongchuan Road, Shanghai 200240, China.

[c] School of Environment, Tsinghua University, Beijing 100084, China.

[d] Department of Earth and Atmospheric Sciences, University of Alberta, Edmonton, Alberta T6G 2E3, Canada

[e] Korea Biochar Research Centre, APRU Sustainable Waste Management Program & Division of Environmental Science and Ecological Engineering, Korea University, Seoul 02841, Korea

* Corresponding author: dan.tsang@polyu.edu.hk

Abstract:

Tailored manipulation of iron speciation has become a critical challenge for the further development of Fe-biochar as an economical and eco-friendly amendment for arsenic (As) immobilization. Herein, a series of Fe-biochars with manipulated iron speciations were fabricated by controlling the carbon structures and pyrolysis conditions. Results revealed that abundant labile-/amorphous-C induced more reductive-Fe(0) formation (10.9 mg g^{-1}) in the Fe-biochar. The high Fe(0) content resulted in the effective As immobilization (4.34 mg g^{-1} As(V) and 7.72 mg g^{-1} As(III)) as evidenced by Pearson correlation coefficient (PCC) analysis. The hierarchical depth distributions of As and Fe on the Fe-biochar caused by the redox reaction and concomitant sorption of As proved the decisive role of Fe(0). An iron-oxide shell (~10−20 nm) with a high arsenic accumulation was revealed on the surface, while deeper within the particles, Fe(0) was found to be associated with elemental As (As(0), up to 19.4%). By contrast, pyrolysis with the stable-/graphitic-C generated more amorphous-Fe (61.9 mg g^{-1}) on the Fe-biochar, which accounted for the high As removal (10.1 mg g^{-1} As(V) and 7.70 mg g^{-1} As(III)) despite the limited Fe(0) content. In comparison to the reductive Fe(0), distinct depth distribution was observed that the As/Fe ratio was marginally changed within 200 nm depth of the amorphous-Fe biochar after As decontamination. Co-precipitation of As with Fe released from amorphous-Fe contributed to this depth distribution, as evidenced by the high correlation between released-Fe and As immobilization capacity (PCC as 0.84−0.95). This study unveiled a crucial role of iron speciation on distinct mechanisms for As removal, guiding the application-oriented design of multifunctional Fe-biochar for broad environmental remediation.

Keywords: Engineering biochar; Arsenic immobilization; Redox reaction; Co-precipitation; Iron transformation; Green and sustainable remediation.

1. Introduction

Arsenic (As) has been recognized as a global environmental concern due to its high toxicity towards human health and ecosystems [1, 2]. Various decontamination methods, including bioremediation, sorption, precipitation, phytoremediation, and electro-coagulation, have been explored to control As pollution in recent years [3-6]. Among these methods, iron-based materials (*e.g.*, ferric hydroxide [7], zero-valent iron (ZVI) [8-10], nano-sized iron/iron oxide [11, 12], and sulfide-modified ZVI [13]) have advantages in the immobilization of As *via* several mechanisms (*i.e.*, electrostatic interaction, monodentate/bidentate complexation, co-precipitation, and redox interactions). In particular, Fe-biochar composites prepared through the pyrolysis of iron-rich biomass or mixture of iron sources and selected biomass waste have attracted growing interest as an effective material for As decontamination [14-16]. This low-cost and eco-friendly procedure can simultaneously realize environmental remediation along with carbon sequestration [17-21].

The key process in the tailored design of Fe-biochar composites is to manipulate the desirable iron speciation during the pyrolysis process to achieve an optimal As immobilization capacity. It is generally acknowledged that reductive gases such as CO and CH_4 are formed during biomass pyrolysis [22] due to the dehydration and decomposition of organic components [23], and these gas intermediates reciprocally reduce the co-present iron species from the +3 state (Fe_2O_3/$Fe(OH)_3$) to +8/3 (Fe_3O_4), +2 (FeO), and 0 (ZVI) [24, 25]. The labile carbon fraction could also directly participate in the thermal reduction of iron oxide [15, 25, 26]. Furthermore, the elevated pyrolysis temperature may facilitate the transformation of amorphous/low-crystallinity iron hydroxides to crystalline iron minerals, even without the participation of carbon [27-29]. We speculate that labile-/amorphous-carbon with a higher degree of volatile compounds possibly induces the formation of lower-state iron, while stable-/graphitic-carbon may primarily change the crystallinity of newly formed iron species with

limited change in the chemical state of iron. Both the reductive-Fe amount (*e.g.*, ZVI) [14, 30] (related to the former process) and the crystallinity of Fe [28] (associated with the latter process) may have repercussions on the As removal capacity and mechanisms by the Fe-biochar composites. Therefore, controlling the fractions of amorphous-/labile-carbon and graphitic-/stable-carbon for the manipulation of iron speciation is probably conducive to fabricating fit-for-purpose Fe-biochar composites for As decontamination. However, current research often overlooks the well-planned design of Fe-biochar synthesis and there is still a lack of corresponding evidence about the influence of carbon species on iron speciation.

Iron species on the biochar govern the immobilization mechanisms and redox reactions of As. For reductive iron species such as ZVI, As(V) and As(III) reduction occurred on the surface of ZVI accompanied by the oxidation of iron [31], where the newly formed ferric oxide could also stabilize As [32, 33]. Meanwhile, As(III) oxidation was found to be triggered by the intermediates formed through interactions between ZVI and O_2 (*e.g.*, Fe(IV) species or hydroxyl radicals [34]) at the solid-liquid interface. The resultant As(V) was subsequently immobilized through electrostatic interaction, complexation, and co-precipitation on the surface of iron minerals [35-37]. Other Fe species (*e.g.*, amorphous ferric hydroxide) contributed to As immobilization *via* direct sorption and co-precipitation [28, 38-40], although As(III) oxidation may happen on the ferric mineral surface in the presence of Fe(II) [36, 41]. Moreover, redox-active moieties (*e.g.*, phenolic −OH and quinoid −C═O) on biochar may drive the redox transformation of As [5, 42]. Direct oxidation of As(III) by the quinoid −C═O on the surface of biochar was reported [43, 44], and electron-donating moieties could indirectly oxidize As(III) together with intermediates (*e.g.*, hydroxyl radicals) produced at the solid-liquid interface [44, 45]. The resultant As(V) was fixed on the iron phases through sorption and complexation [5, 46, 47]. The variations in both reaction sites and reaction sequence of redox and sorption may cause a “layered distribution” of As and Fe with different valence states. In

this study, the unprecedented revealing of this hierarchical distribution of Fe-biochar composites with amorphous-Fe or reductive-Fe can provide insightful details about the As immobilization mechanisms.

Herein, we fabricated a series of Fe-biochar composites with varying iron speciations by controlling the co-pyrolyzed carbon phases (*i.e.*, ranging from labile-/amorphous-C to stable-/graphitic-C) and pyrolysis conditions. Immobilization capacities and mechanisms of these Fe-biochar composites for As(V) and As(III) were analyzed. The main objectives of this study were to scrutinize (i) the roles of different carbon fractions on regulating the Fe speciation in the Fe-biochar composites, and (ii) the hierarchical depth distributions of As and Fe on the Fe-biochar composites after As immobilization. Using multiple characterization methods including semi-quantitative X-ray diffraction (Q-XRD), depth-profiling X-ray photoelectron spectroscopy (XPS) analysis, Raman spectroscopy, and Pearson correlation coefficient (PCC) analysis, we unveiled the vital roles of carbon structures in manipulating the resultant Fe speciation, and the distinct depth distributions of Fe and As provided direct evidence for the underlying mechanisms of As immobilization with the Fe-biochar composites.

2. Materials and Methods

2.1 Chemicals and Raw Materials

All chemicals used in this study were of analytical grade. Detailed information is provided in the **Supporting Information** (**SI**, **Text S1**). A mixture of locally available light yard waste (LYW), collected from EcoPark in Hong Kong, was selected as the raw biomass. This biomass was crushed to pass through a 120-mesh sieve (particle size < 0.125 mm) and dried at 60 ℃ for 24 h before pyrolysis.

2.2 Preparation of Fe-biochars

Four biochars (BC400, BC550, BC700, and BC850) pyrolyzed at different temperatures

(*i.e.*, 400, 550, 700, and 850 °C) were first prepared through the slow pyrolysis of LYW under N_2 atmosphere for 1 h with a ramping rate of 10 °C min^{-1}. These temperatures were selected to obtain biochars with varying carbon structures, including transition char, amorphous char, composite char, and graphitic char [48]. The basic properties of the resulting biochars are summarized in **Text S2** and **Figures S1**−**S2**. Then, 20 g of each biochar was added into 200 mL $FeCl_3$ solution (10 g Fe L^{-1}) (biochar-to-Fe mass ratio as 10:1). Each mixture was stirred with a magnetic stirrer at 200 rpm for 24 h, dried at 60 °C for over 72 h, and then crushed to pass a 120-mesh sieve and stored in a dry container before its second pyrolysis. The resulting Fe-biochar composites were denoted as BCX-Fe, where X indicates the first pyrolysis temperature.

Two series of Fe-biochars (a total of 7) were designed. Firstly, four Fe-biochar composites (BC400-Fe, BC550-Fe, BC700-Fe, and BC850-Fe) were pyrolyzed at 850 °C for 1 h to evaluate the potential of varied carbon structures to form a diverse spectrum of reduced Fe species. A higher pyrolysis temperature over 800 °C can lead to the formation of ZVI with the reduction by biochar matrix [15]. These four Fe-biochar composites with rich reductive-Fe were named BCX-Fe-850, where X indicates the first pyrolysis temperature. Secondly, to study the variations in the Fe species with initially stable-/graphitic-carbon, only BC850-Fe was used to fabricate the second series of Fe-biochars through pyrolysis at 400 °C, 550 °C, and 700 °C for 1 h. Due to the high stability of BC850, these three pyrolytic temperatures might result in relatively high contents of amorphous-Fe on the Fe-biochar composites with limited Fe valence transformation. This series of Fe-biochar composites with high amorphous-Fe contents were named BC850-Fe-X, where X was the second pyrolysis temperature. The design and preparation procedures for all seven Fe-biochar composites are summarized in **Figure S1**, and all these Fe-biochar composites were stored in a sealed container before further use.

2.3 Characterization

Detailed information about X-ray diffraction (XRD, Rigaku SmartLab-9kW-advance), X-ray photoelectron spectroscopy (XPS, Thermo Scientific Nexsa), Raman spectrometer (Renishaw, UK), and other characterization methods can be found in **Text S3**. Quantitative X-ray diffraction (Q-XRD) was performed to evaluate the content of different Fe species in the Fe-biochar composites, using CaF_2 as the internal standard and typical Fe minerals as quality control (**Text S4** and **Figures S3**–**S4**). Various Fe extraction methods were also conducted to quantify the Fe-speciation in the Fe-biochar composites, including the soluble-, reducible-, and extractable-Fe, which are explained in **Text S4**.

2.4 As Immobilization Mechanisms and Hierarchical Depth Distributions

The immobilization capacities of all Fe-biochar composites for both As(V) and As(III) were evaluated through batch experiments. Briefly, 0.1 g of selected Fe-biochar composite was added into a 50 mL centrifuge tube containing 50 mL of 60 mg L^{-1} As(III) or As(V) solution, which was prepared by dissolving an appropriate amount of $NaAsO_2$ or $Na_2HAsO_4{\cdot}7H_2O$, respectively, in a 20 mM NaCl background solution. The resulting concentrations of As(III) or As(V) were within the maximum concentrations of As wastewater generated by smelting, metallurgical plant, or soil washing [49-51]. The above mixtures were shaken at 250 rpm under 25 ± 1 °C without light irradiation until equilibrium was reached (48 h). All experiments were conducted in triplicate, and the detailed sampling procedures are described in **Text S5**. The methods for quantification of As(III)/As(V) and Fe(II)/Fe(III), and the characterization of the Fe-biochar composites after As immobilization is also available in **Text S5**. The Pearson correlation coefficient (PCC) was calculated to assess the vector similarity between the physicochemical properties, Fe-speciation, and As removal capacities of Fe-biochars with the supplement of extra 11 Fe-biochar composites as elaborated in **Text S6**. Depth profiling XPS analysis was used to evaluate the hierarchical depth distributions of As and Fe on typical Fe-biochar composites after As(III) or As(V) removal from the solution. An argon gun was used

to etch the surface of Fe-biochar composites with a standard sputter rate before XPS analysis, and thus the distributions and chemical properties of As and Fe under the different depths of Fe-biochar composites could be evaluated. Detailed information about the depth profiling XPS can be found in **Text S7**.

3. Results and Discussion

3.1 Manipulation of Iron Speciation in Fe-biochar

After the designed fabrication (**Figure S1**), the total Fe contents of the resulting seven Fe-biochar composites ranged between 81.4–90.0 mg g^{-1} (**Table S1**), and various Fe speciations were observed according to the XRD analysis (**Figure 1a**). The use of second pyrolysis temperature of 850 °C induced the formation of wustite (FeO) and magnetite (Fe_3O_4), while ZVI was only formed on BC400-Fe-850 and BC550-Fe-850 that contained abundant labile-C. Based on semi-quantitative Q-XRD analysis, the highest ZVI content of 10.9 mg g^{-1} was found in the BC400-Fe-850, which also had the lowest amorphous-Fe content (3.11 mg g^{-1}) (**Figures 1b**, **S4**, and **Table S2**). These results implied that labile carbon in the low-temperature biochars promoted the formation of reductive-Fe (*e.g.*, ZVI), whereas stable/graphitic carbon in the high-temperature biochars failed to act similarly as an effective reducing agent.

For the Fe-biochar composites produced *via* pyrolysis of BC850-Fe at a lower pyrolysis temperature, only magnetite (Fe_3O_4) (BC850-Fe-700 and BC850-Fe-550) and hematite (Fe_2O_3) (BC850-Fe-400) were formed, and no completely reductive-Fe species (*i.e.*, ZVI and FeO) were observed (**Figure 1a**). XPS analysis showed that these three Fe-biochar composites exhibited slightly higher Fe(III) proportion (28.0-30.2%) than those produced at 850 °C (25.5-27.6%) (**Figure S5**), further suggesting the limited Fe reduction process. According to the Q-XRD analysis, amorphous-Fe was the dominant Fe-species in BC850-Fe-400, and its amount decreased from 61.9 mg g^{-1} to 28.9 mg g^{-1} with the increase of second pyrolysis temperature

to 700 °C (**Figures 1b**, **S4**, and **Table S2**). The amorphous-Fe contents in these Fe-biochar composites were much higher than those produced at second pyrolysis temperature of 850 °C (< 10.3 mg g^{-1}). These results indicated that graphitic-C only promoted the formation of high-valence Fe minerals and amorphous-Fe during the co-pyrolysis, which was supported by other recent findings [52]. SEM-EDX analysis revealed that similar and spherical Fe particles were attached on the biochar surface in all Fe-biochar composites despite the difference in Fe speciations (**Figures S6**–**S8**), indicating that the surface morphology of these composites might play a less significant role in the As decontamination compared with Fe-species.

The driving role of carbon structures in tuning the Fe speciation was further verified using Raman spectroscopy, Fourier transform infrared spectroscopy (FTIR), and elemental analysis (EA). An increased value of A_d/A_g (*i.e.*, area ratio between D-band and G-band from Raman spectroscopy) from 1.62–1.82 to 2.36–2.38 (**Figures 1c** and **S2**), a decreased surface functionality (**Figures 1d** and **S2**), and a reduced O/C atomic ratio from 0.24 to 0.17 (**Figures S2** and **S9**) were observed after the pyrolysis of BC400-Fe/BC550-Fe at 850 °C. This corresponded to the transformation from labile-/aliphatic-C to stable-/aromatic-C during the second pyrolysis at a higher temperature [23, 53]. This carbon transformation would facilitate the carbothermal reduction process [25], leading to a higher content of reductive-Fe in the resulting Fe-biochar composites (**Figures 1a** and **1b**). However, limited carbon transformation occurred on the graphitic-C (BC850-Fe) during its second pyrolysis, as indicated by the negligible changes in the A_d/A_g ratio and H/C atomic ratio (**Figures 1c**, **S2**, and **S9**). The higher stability of BC850-Fe accounted for the limited carbon transformation and the high proportion of amorphous-Fe on BC850-Fe-700/550/400 with a limited reducing process. A peak of Fe–OH/Fe–O (~557 cm^{-1}) was observed on BC850-Fe-400 (**Figure 1d**), which could be attributed to amorphous iron hydroxide [54, 55], further confirming its high content of amorphous iron. Despite their distinct carbon structures before the second pyrolysis process, all seven Fe-

biochar composites displayed similar final carbon properties (*i.e.*, surface functionality) after variable carbon transformation processes (**Table S1**, **Figures 1c-d**, and **S9-11**). This suggested that the impact of the carbon matrix may be secondary and indirect when comparing the As immobilization capacities of these Fe-biochar composites.

The porosity change of Fe-biochar composites also supported the different carbon transformations with Fe (**Table S1** and **Figures S12** and **S13**). There was an apparent increase of the specific surface area (SSA) from 2.62–5.74 $m^2\ g^{-1}$ (BC400/550/700/850-Fe) to 308–373 $m^2\ g^{-1}$ (BC400/550/700/850-Fe-850) with an increased pore volume (PV) from 0.007–0.018 $cm^3\ g^{-1}$ to 0.018–0.056 $cm^3\ g^{-1}$ after the second pyrolysis at 850 °C. The carbothermal reduction process of Fe appeared to consume the labile fraction in the carbon matrix and thus formed a more porous structure in the resulting Fe-biochar composites. By contrast, there were limited transitions of SSA from 5.74 $m^2\ g^{-1}$ (BC850-Fe) to 7.83–10.7 $m^2\ g^{-1}$ (BC850-Fe-400/550/700) and PV from 0.018 $cm^3\ g^{-1}$ to 0.014–0.020 $cm^3\ g^{-1}$ on graphitic-C (BC850-Fe) after the second pyrolysis at lower temperatures, confirming the negligible transformation of stable/graphitic carbon with Fe. Overall, labile-/amorphous-C under a higher temperature in the second pyrolysis resulted in a Fe-biochar composite containing more reductive-Fe species (*e.g.*, ZVI), while stable-/graphitic-C substrate (BC850) produced more amorphous-Fe species after the second pyrolysis. This remarkable difference of Fe-speciation in these Fe-biochar composites would play a key role in governing variable As immobilization capacities.

3.2 Arsenic Immobilization Capacities

The immobilization capacities of the two series of Fe-biochar composites for both As(V) and As(III) were explored (**Figures 2a** and **2b**). Among those Fe-biochar composites containing more reductive-Fe (*i.e.*, BC400/550/700/850-Fe-850), BC400-Fe-850 showed the highest immobilization capacities for both As(V) (4.34 mg g^{-1}) and As(III) (7.72 mg g^{-1}). The As(V) and As(III) removal capacity declined markedly to 0.29 mg g^{-1} and 1.18 mg g^{-1},

225 respectively, when the first pyrolysis temperature was raised to 850 °C (BC850-Fe-850) (**Table**
226 **S3**). Interestingly, Fe-biochar composites with more amorphous-Fe species (*i.e.,* BC850-Fe-
227 400/550/700) also showed considerable removal capacities for both As(V) and As(III) despite
228 the absence of ZVI. About 1.68–1.82 mg g^{-1} As(V) and 2.97–2.98 mg g^{-1} As(III) were removed
229 by BC850-Fe-550 and BC850-Fe-700 after 48-h immobilization, and BC850-Fe-400
230 effectively immobilized 11.0 mg g^{-1} As(V) and 7.70 mg g^{-1} As(III) (**Table S3**). BC850-Fe-400
231 could provide an even higher As immobilization capacity than BC400-Fe-850 (4.34 mg g^{-1} for
232 As(V) and 7.72 mg g^{-1} for As(III)), which had the highest ZVI content. It is worth noting that
233 pristine BC850 with high SSA (201 m^2 g^{-1}, **Figure S13**) and similar carbon properties (**Figure**
234 **S2**) showed a limited immobilization capacity for both As(V) and As(III), indicating that the
235 Fe species instead of carbon properties primarily determined the As removal performance.
236 Both series of Fe-biochar composites with variable Fe species (*i.e.,* reductive-Fe and
237 amorphous-Fe) could accomplish considerable As decontamination, which was close to those
238 in relevant studies with similar Fe speciation and Fe loading (**Text S8** and **Table S4**); however,
239 the dominant immobilization mechanisms would be distinct. For instance, the ZVI content may
240 contribute to As(V) and As(III) removal by Fe(0)-biochar [14, 30], while direct sorption and
241 co-precipitation might dominate As immobilization for the Fe-biochar possessing abundant
242 amorphous Fe [28].
243 **3.3 Role of ZVI on the As immobilization by Reductive-Fe Rich Biochar**
244 A slight increase in the pH value from ~7.8 to 8.3–8.6 was found in the As(V) solution after
245 the addition of Fe-biochar composites containing high proportion of reductive-Fe (BCX-Fe-
246 850) (**Figure 2a**). As the intrinsic pH of these Fe-biochar composites (7.3–7.5, **Table S1**) was
247 lower than that of the solution, the increased solution pH may be attributed to the consumption
248 of H^+ during the As(V) reduction by reductive-Fe (**eq. 1**) [14]. No Fe dissolution and only
249 limited soluble As(III) were detected (< 0.15 mg g^{-1}) after the As immobilization (**Figure S14**),

indicating that this reaction might be an interfacial process instead of a solution reaction [9]. As(V) was reduced on the ZVI surface and then directly immobilized as the Fe-As surface complex [14, 56], which could be evidenced by a well-overlapping distribution of Fe and As observed in the SEM-EDX mapping (**Figure S15**).

$$HAsO_4^{2-}\ (As(V)) + 2e^- + 3H^+ \rightarrow H_2AsO_3^-\ (As(III)) + H_2O \quad (1)$$

A slight increase in the solution pH from 7.7 to 8.1–8.2 was detected after As(III) immobilization by BC400-Fe-850 and BC550-Fe-850, while a marginally increased or even a decreased pH occurred for BC700-Fe-850 and BC850-Fe-850 (**Figure 2b**). This phenomenon could be attributed to As(III) oxidation with simultaneous H^+ generation (**eq. 2**). About 0.65–5.48 mg g^{-1} of As(V) was formed after adding these four Fe-biochar composites (**Figure S14**), and BC700-Fe-850 and BC850-Fe-850 reached relatively high soluble As(V) concentrations of 3.34 mg g^{-1} and 5.48 mg g^{-1}, respectively. The carbon phase in Fe-biochar may be the primary oxidizing moieties for As(III) [44] in view of the remarkable electron-accepting capacity of high-temperature biochar [53, 57]. As(III) oxidation by ZVI-derived intermediates, such as Fe(IV) and hydroxyl radicals [34, 58], was possbily less critical considering relatively low As(V) concentrations in BC400/550-Fe-850 (*i.e.*, high ZVI content) as compared with BC700/850-Fe-850 (*i.e.*, low ZVI content). An overlapping elemental distribution of Fe and As was also observed on BC400-Fe-850 after As(III) removal (**Figure S15**), corroborating the indispensable role of Fe-As combination in As(III) immobilization. Both the redox reaction with carbon fraction and the sorption onto Fe-phases contributed to the As(III) removal by the Fe-biochar enriched with reductive-Fe.

$$H_2AsO_3^-\ (As(III)) - 2e^- + H_2O \rightarrow HAsO_4^{2-}\ (As(V)) + 3H^+ \quad (2)$$

To verify the critical role of ZVI, several Fe-biochar composites with different reductive-Fe loadings (*i.e.*, ZVI and FeO) and similar pH values were designed (**Text S6**, **Tables S5-6**, and **Figures S16-17**). PCC analysis between the As removal capacities and Fe speciation of

these Fe-biochars showed that the As(V) and As(III) removal capacities were positively related to the contents of ZVI (r = 0.98) and FeO (r = 0.90–0.91), but negatively associated with the amount of Fe_3O_4 (r = -0.97) (**Figures 2c** and **S18-19**). In addition, the As removal capacities were highly correlated with the reducible-Fe content (r = 0.95–0.96), as determined by the hydroxylamine-HCl extraction method [59, 60] (**Text S4**). A nearly linear relationship (R^2= 0.90–0.92, **Figure S20**) could be well established between As removal capacity and reducible-Fe fraction, reinforcing the importance of ZVI (PCC of 0.80 between ZVI and reducible-Fe, **Figure 2e** and **Table S7**). Moreover, Q-XRD revealed a decrease of ZVI from 10.91 mg g^{-1} to 6.51–7.91 mg g^{-1} on BC400-Fe-850 with a concomitant increase of amorphous-Fe from 3.11 mg g^{-1} to 11.4–16.9 mg g^{-1} during the As immobilization process (**Figure S21**). Overall, the formation of ZVI related to the labile-C was the critical component for an efficient As removal by Fe-biochar composites with rich reductive-Fe.

3.4 Core-shell Structure Generated by Redox Reactions between Arsenic and ZVI

To explore the As immobilization mechanisms of Fe-biochar composites, an advanced depth profiling XPS analysis was conducted on BC400-Fe-850, which was the typical reductive-Fe rich biochar. Results showed that BC400-Fe-850 was covered by an iron-oxide layer (~10–20 nm) after the reaction with As(V) or As(III) with no Fe(0) (**Figures 3a**–**b** and **S22**). Fe(0) could only be detected at the depths of 20–50 nm, and its proportion increased to 6.2% and 9.9% at the 200 nm depth after As(V) and As(III) removal, respectively. The atomic ratio of O/Fe also suggested the formation of an oxide shell on the ZVI surface (**Figures 3a**–**b** and **S23**). Higher O/Fe atomic ratios of 3.8–6.5 were found on Fe-biochar composites after As(V) decontamination within the first ~20 nm from the surface, and they decreased to 2.8–3.4 in the depth range between 20 to 200 nm. A similar transition was found after As(III) immobilization that the O/Fe atomic ratios as 3.4–8.1 were found within the ~20 nm from the surface, and then declined to 2.6–2.8 from 20 nm to 200 nm.

Besides, As accumulation also varied over depth. High As/Fe atomic ratios were observed within 0–10 nm of the surface of BC400-Fe-850 (0.8–1.2 for As(V) and 0.7–1.5 for As(III)), and the ratios decreased to 0.6–0.7 when depth approached below 20 nm. No apparent change of As/Fe atomic ratios could be observed between a depth range of 20-200 nm (0.6–0.7 for As(V) and 0.6 for As(III)).

The proportion of different As species (*i.e.*, As(V), As(III), and As(0)) varied in different layers of BC400-Fe-850 (**Figures 4a** and **4b**). For As(V) immobilization, As(V) was the primary As species on the surface (92.7%, **Figure 4a**), and its proportion gradually decreased to 42.8% with an increasing depth to 200 nm (**Figures 4a** and **S24**). Meanwhile, the proportion of As(III) and As(0) showed a noticeable increase to ~37.8% and 19.4% (**Figure 4a**), respectively. These results provided credible evidence for the critical role of ZVI in As(V) immobilization (**Figure 4c**). Specifically, the reduction of As(V) to As(III) and even As(0) through As–Fe binding happened after the intraparticle diffusion of As into the ZVI layer. The As(V) reduction led to the formation of the iron-oxide on the surface of ZVI, and this newly formed iron oxide could effectively attract As(V) and As(III) through electrostatic interactions and surface complexation with Fe (≡Fe–O–As(III/V)) [31, 61]. A core-shell structure was formed during the As removal process, *i.e.*, ZVI coordinating with As(0)/As(III) acted as the core, and amorphous iron oxide complexing with As(V)/As(III) was the outside-shell (**Figure 4c**). The higher As/Fe atomic ratios (0.8–1.2) within the first ~10 nm from the surface indicated the preferable As immobilization onto the surface oxide shell compared with the inner reduction and adjoint complexation with ZVI core. For As(III) removal by BC400-Fe-850 (**Figures 4b** and **S24**), the appearance of As(0) (13.9–26.0%) below 10 nm suggested a similar As intraparticle diffusion and reduction process by Fe(0). As(V) was mainly observed on the outside layer of BC400-Fe-850 (36.6%) during the As(III) immobilization and decreased to 12.0–18.4% at 10–200 nm depth (**Figures 4b** and **S24**), indicating that As(III) was probably

oxidized by the surface functional groups of biochar [44, 62] or intermediates (*e.g.*, Fe(IV) and hydroxyl radicals [34, 58]) and then stabilized on the iron-oxide shell.

3.5 Acidity from Amorphous-Fe Rich Biochar Facilitated Arsenic Decontamination

Unlike the Fe-biochar composites rich in reductive-Fe (*i.e.*, BC400/550/700/850-Fe-850), an apparent decrease in solution pH was found after the addition of Fe-biochar composites containing a higher fraction of amorphous-Fe (BC850-Fe-400/550/700) during both As(V) (from 7.6 to 3.1–3.2) and As(III) (from 8.0 to 3.1–3.2) immobilization. This phenomenon was plausibly due to the high acidity of these Fe-biochar composites (pH = 2.9–3.1, **Table S1**). The hydrolysis process of amorphous-Fe [63] was evidenced by the negative relationship between pH and amorphous-Fe content (PCC of -0.92, **Figure 2e** and **Table S7**).

To identify the role of acidity from amorphous-Fe, the initial solution pH was adjusted to 10.2–10.4 before the addition of amorphous-Fe rich composites (**Figure S18**). Compared with the unadjusted experiments, the pH after As immobilization by Fe-biochar composites increased to 3.4–3.8, and the immobilization capacities slightly changed to 1.73–10.1 mg g^{-1} for As(V) and 2.50–7.10 mg g^{-1} for As(III). The lower As immobilization capacity of BC850-Fe-400 at a higher pH confirmed the importance of acidity during the As immobilization process. The acidic condition could facilitate Fe dissolution and enhance electrostatic interactions between Fe-biochar and As [5, 64], thus improving their As immobilization capacities. Results from the adjusted pH experiments also indicated that the amorphous-Fe could effectively buffer the solution alkalinity and maintain an acidic environment, leading to a considerable immobilization capacity for As even at a high initial pH. In addition, a low initial pH (3.2–3.3) was also set for the Fe-biochar composites containing reductive-Fe to test the As immobilization capacities, where improved removal was found for both As(V) (0.85–12.1 mg g^{-1} > 0.29–4.34 mg g^{-1}) and As(III) (1.24–9.78 mg g^{-1} > 1.19–7.72 mg g^{-1}) (**Figure S18**). These results indicated that the As immobilization capacity of Fe-biochar would be inhibited

by the limited acidity due to the less amorphous-Fe content.

3.6 Arsenic Removal *via* Co-precipitation with the Fe Released from Amorphous-Fe Rich Biochar

Despite the strengthened As immobilization by the acidity, the soluble Fe released from these amorphous-Fe rich composites might determine the As removal. There was no significant correlation between different iron minerals (*i.e.*, amorphous-Fe, Fe_2O_3, and Fe_3O_4) and As removal capacities (r=-0.51–0.17, p>0.05, **Figures 2d** and **S25**) based on the PCC analysis of these Fe-biochar composites (**Text S6**). In contrast, the As removal capacities were highly relevant to extractable-Fe (r = 0.93–0.95), soluble-Fe (r = 0.91–0.94), and reducible-Fe (r = 0.84–0.86) (**Figures 2d** and **S25**), determined through different extraction methods (**Text S4**). These Fe fractions represented the active Fe in amorphous-phase that could be readily released into the solution through chelation by dissolved organic carbon from biochar [65] or reduction to soluble Fe(II) by reductive biochar moieties [66]. There was a linear relationship (R^2 = 0.71–0.90) between the As removal amount and the Fe content of Fe-biochar composites (**Figure S26**). The released Fe ions can co-precipitate with As to form As-Fe amorphous complexes on carbon [28, 67], which was corroborated by the homogeneous distribution of As on the biochar surface (**Figure S15**), the increase in amorphous-Fe content (**Figure S21**), and the decline in the soluble Fe concentration after As immobilization (**Figure S27**). Limited As(V) reduction was induced (< 0.5 mg g^{-1}, **Figure S14**) by amorphous-Fe rich biochar composites, but As(III) oxidation could possibly be achieved due to oxidizing capacity of both biochar [62] and ferric minerals [41, 46, 68] during the co-precipitation process (**Figure S12**). More soluble Fe(II) was formed after As(III) removal compared with As(V) removal, evidencing the oxidation of As(III) along with Fe(III) reduction (**Figure S27**). In short, Fe released from the amorphous-Fe was a critical factor for As removal by Fe-biochar with abundant amorphous-Fe.

3.7 Fixed Layered Composition of Arsenic and Iron by the Co-precipitation Process

BC850-Fe-400 was selected as the representative Fe-biochar composites with rich amorphous-Fe to evaluate the depth distribution of As and Fe generated through the co-precipitation process. There was no noticeable change of O/Fe atomic ratio at different depths of BC850-Fe-400 after As(V) (2.9–4.1) or As(III) (3.0–3.8) removal, and the Fe valence remained constant at different layers (**Figures 3c**–**d** and **S23**). The As/Fe atomic ratios also kept stable in BC850-Fe-400 after As(V) (~1.0–1.1) or As(III) (~0.8) immobilization, and As(V) was the dominant form on BC850-Fe-400 in both systems (76.2–100% for As(V) immobilization and 57.5–87.8% for As(III) immobilization) (**Figures 4d**–**e** and **S24**). The fairly stable ratio and speciation of As/Fe indicated the possible formation of an amorphous scorodite-like mineral ($FeAsO_4$, Fe/As ~1) or ferrous arsenate ($FeHAsO_4$, Fe/As ~1) on BC850-Fe-400, reaffirming the As removal by the co-precipitation process (**Figure 4f**). Accordingly, lower As/Fe atomic ratios were found after As(III) removal as the As(III) should be oxidized to As(V) with the consumption of extra Fe before co-precipitation. A small proportion of Fe(0) was found at the deep depth (200 nm) of BC850-Fe-400, which might be attributed to the long-time sputtering process during depth profiling [69].

3.8 Comparison between the Reductive-Fe-Biochar and Amorphous-Fe-Biochar

Various primary Fe-species on Fe-biochar caused the different immobilization processes, leading to a distinct hierarchical distribution of As and Fe in the biochar composites. Core-shell structure on the reductive-Fe-biochar after As immobilization offered plausible evidence of combined redox and sorption process for As in the presence of ZVI. By contrast, a marginally changed As/Fe ratio and steady compositions of As and Fe were found in the amorphous-Fe-biochar after As removal, corresponding to the co-precipitation process.

The intrinsic advantages/disadvantages of reductive-Fe-biochar and amorphous-Fe-biochar for As immobilization can be inferred in light of the varying removal mechanisms and hierarchical depth distributions. For reductive-Fe-biochar, highly toxic As(III) was

encapsulated inside the iron oxide shell during the immobilization process; however, the stability of this iron oxide shell remained uncertain. Dissolution of the amorphous oxide layer might represent a potential risk of As(III) remobilization into the environment. The fate of elemental As combined with Fe(0) was also unclear. Thus, future studies are required to prove the long-term stability of As fixed on the reductive-Fe-biochars under seasonally changeable field-relevant conditions. For the amorphous-Fe-biochars, the oxidative transformation of As(III) to low toxicity As(V) and the high As removal capacity offered apparent advantages, especially considering the lower energy input for biochar composites production. However, the unintended environmental risk of the indigenous acidity associated with released Fe ions and the competition of coexisting anions (*e.g.*, PO_4^{3-}) during the co-precipitation process still mandate further investigation.

4. Conclusions

In this study, we proposed a hypothesis-driven manipulation of Fe speciation in the design of Fe-biochar composites, and the underlying mechanisms and hierarchical depth distributions of Fe and As were scrutinized. Our results evidenced that reductive-Fe species, which mainly immobilized As through redox reaction and sorption/complexation, were formed at a high pyrolysis temperature with co-pyrolyzed labile-/amorphous-C. In contrast, amorphous-Fe species were primarily produced with stable-/graphitic-C and they removed As through co-precipitation with released Fe. Our study highlighted the key roles of carbon structures in the regulation of Fe species in the biochar composites. Labile-/amorphous-C and stable/graphitic-C led to distinct ZVI and amorphous-Fe contents in the resulting Fe-biochar composites during the pyrolysis process. Therefore, understanding and customizing the carbon structures is a prerequisite for fabricating biochar composites with the targeted Fe species. The hierarchical distributions analyzed in this study offered unprecedented high-resolution details on the As

removal mechanisms by different Fe-biochar composites, thus providing direct evidence about As immobilization through co-precipitation and/or sorption with redox reaction. Overall, these findings can guide our rational design of multifunctional Fe-biochar composites for broader and fit-for-purpose applications, which are indispensable for actualizing sustainable environmental remediation together with global decarbonization.

Supporting Information

The supporting information including 8 texts, 7 tables, and 27 figures about the basic physicochemical properties of the pristine biochars, characterization methods (SEM, Raman, XPS, and XRD, *etc.*) of the prepared Fe-biochar, analytical methods for As removal, quantitative identification of Fe speciation, Pearson correlation analysis, supplementary tables/figures about the Fe-biochar properties, As removal performance, and depth-profiling XPS analysis, *etc.*, can be found online.

Acknowledgment

We appreciate the financial support from the Hong Kong Environment and Conservation Fund (Project 101/2020) and Hong Kong Research Grants Council (PolyU 15222020) for this study. We acknowledge the equipment support provided by the University Research Facility in Chemical and Environmental Analysis (UCEA) of the Hong Kong Polytechnic University.

References:

[1] Z. Song, S. Garg, J. Ma, T.D. Waite, Selective Arsenic Removal from Groundwaters Using Redox-Active Polyvinylferrocene-Functionalized Electrodes: Role of Oxygen, Environ. Sci. Technol. 54(19) (2020) 12081-12091.

[2] Y. Shi, W. Chen, S. Wu, Y. Zhu, Anthropogenic Cycles of Arsenic in Mainland China: 1990–2010, Environ. Sci. Technol. 51(3) (2017) 1670-1678.

[3] S. Alka, S. Shahir, N. Ibrahim, M.J. Ndejiko, D.-V.N. Vo, F.A. Manan, Arsenic removal technologies and future trends: A mini review, Journal of Cleaner Production 278 (2021) 123805.

[4] B. Liu, K.-H. Kim, V. Kumar, S. Kim, A review of functional sorbents for adsorptive removal of arsenic ions in aqueous systems, J. Hazard. Mater. 388 (2020) 121815.

[5] R. Amen, H. Bashir, I. Bibi, S.M. Shaheen, N.K. Niazi, M. Shahid, M.M. Hussain, V. Antoniadis, M.B. Shakoor, S.G. Al-Solaimani, H. Wang, J. Bundschuh, J. Rinklebe, A critical review on arsenic removal from water using biochar-based sorbents: The significance of modification and redox reactions, Chem. Eng. J. 396 (2020) 125195.

[6] L. Weerasundara, Y.-S. Ok, J. Bundschuh, Selective removal of arsenic in water: A critical review, Environ. Pollut. 268 (2021) 115668.

[7] X. Guan, J. Wang, C.C. Chusuei, Removal of arsenic from water using granular ferric hydroxide: Macroscopic and microscopic studies, J. Hazard. Mater. 156(1) (2008) 178-185.

[8] T.K. Das, A.N. Bezbaruah, Comparative study of arsenic removal by iron-based nanomaterials: Potential candidates for field applications, Sci. Total Environ. 764 (2021) 142914.

[9] W. Yan, M.A.V. Ramos, B.E. Koel, W.-x. Zhang, As(III) Sequestration by Iron Nanoparticles: Study of Solid-Phase Redox Transformations with X-ray Photoelectron Spectroscopy, The Journal of Physical Chemistry C 116(9) (2012) 5303-5311.

[10] F. Sun, K.A. Osseo-Asare, Y. Chen, B.A. Dempsey, Reduction of As(V) to As(III) by commercial ZVI or As(0) with acid-treated ZVI, J. Hazard. Mater. 196 (2011) 311-317.

[11] L. Otero-González, S.V. Mikhalovsky, M. Václavíková, M.V. Trenikhin, A.B. Cundy, I.N. Savina, Novel nanostructured iron oxide cryogels for arsenic (As(III)) removal, J. Hazard. Mater. 381 (2020) 120996.

[12] J.W. Brockgreitens, F. Heidari, A. Abbas, Versatile Process for the Preparation of Nanocomposite Sorbents: Phosphorus and Arsenic Removal, Environ. Sci. Technol.

54(14) (2020) 9034-9043.
[13] P. Singh, P. Pal, P. Mondal, G. Saravanan, P. Nagababu, S. Majumdar, N. Labhsetwar, S. Bhowmick, Kinetics and mechanism of arsenic removal using sulfide-modified nanoscale zerovalent iron, Chem. Eng. J. 412 (2021) 128667.
[14] S. Bakshi, C. Banik, S.J. Rathke, D.A. Laird, Arsenic sorption on zero-valent iron-biochar complexes, Water Res. 137 (2018) 153-163.
[15] Y. Sun, I.K.M. Yu, D.C.W. Tsang, X. Cao, D. Lin, L. Wang, N.J.D. Graham, D.S. Alessi, M. Komárek, Y.S. Ok, Y. Feng, X.-D. Li, Multifunctional iron-biochar composites for the removal of potentially toxic elements, inherent cations, and hetero-chloride from hydraulic fracturing wastewater, Environment International 124 (2019) 521-532.
[16] Y. Zou, X. Wang, A. Khan, P. Wang, Y. Liu, A. Alsaedi, T. Hayat, X. Wang, Environmental Remediation and Application of Nanoscale Zero-Valent Iron and Its Composites for the Removal of Heavy Metal Ions: A Review, Environ. Sci. Technol. 50(14) (2016) 7290-7304.
[17] J. Lehmann, A handful of carbon, Nature 447(7141) (2007) 143-144.
[18] J. Lehmann, Bio-energy in the black, Front. Ecol. Environ. 5(7) (2007) 381-387.
[19] A. Rawal, S.D. Joseph, J.M. Hook, C.H. Chia, P.R. Munroe, S. Donne, Y. Lin, D. Phelan, D.R.G. Mitchell, B. Pace, J. Horvat, J.B.W. Webber, Mineral-Biochar Composites: Molecular Structure and Porosity, Environ. Sci. Technol. 50(14) (2016) 7706-7714.
[20] L. Wang, D. O'Connor, J. Rinklebe, Y.S. Ok, D.C.W. Tsang, Z. Shen, D. Hou, Biochar Aging: Mechanisms, Physicochemical Changes, Assessment, And Implications for Field Applications, Environ. Sci. Technol. 54(23) (2020) 14797-14814.
[21] S.M. Shaheen, N.K. Niazi, N.E.E. Hassan, I. Bibi, H.L. Wang, D.C.W. Tsang, Y.S. Ok, N. Bolan, J. Rinklebe, Wood-based biochar for the removal of potentially toxic elements in water and wastewater: a critical review, Int. Mater. Rev. 64(4) (2019) 216-247.
[22] W. Chen, W. Farooq, M. Shahbaz, S.R. Naqvi, I. Ali, T. Al-Ansari, N.A. Saidina Amin, Current status of biohydrogen production from lignocellulosic biomass, technical challenges and commercial potential through pyrolysis process, Energy 226 (2021) 120433.
[23] X. Xiao, B. Chen, Z. Chen, L. Zhu, J.L. Schnoor, Insight into Multiple and Multilevel Structures of Biochars and Their Potential Environmental Applications: A Critical Review, Environ. Sci. Technol. 52(9) (2018) 5027-5047.

[24] J. Yang, N. Cai, Z. Li, Hydrogen production from the steam-iron process with direct reduction of iron oxide by chemical looping combustion of coal char, Energy & Fuels 22(4) (2008) 2570-2579.
[25] Y.Shen, Carbothermal synthesis of metal-functionalized nanostructures for energy and environmental applications, Journal of Materials Chemistry A 3(25) (2015) 13114-13188.
[26] A. Cazetta, O. Pezoti, K.C. Bedin, T.L. Silva, A. Paesano Junior, T. Asefa, V.C. Almeida, Magnetic Activated Carbon Derived from Biomass Waste by Concurrent Synthesis: Efficient Adsorbent for Toxic Dyes, ACS Sustainable Chemistry & Engineering 4(3) (2016) 1058-1068.
[27] A. Arinchtein, R. Schmack, K. Kraffert, J. Radnik, P. Dietrich, R. Sachse, R. Kraehnert, Role of Water in Phase Transformations and Crystallization of Ferrihydrite and Hematite, ACS Applied Materials & Interfaces 12(34) (2020) 38714-38722.
[28] Y. Yu, Z. Xu, X. Xu, L. Zhao, H. Qiu, X. Cao, Synergistic role of bulk carbon and iron minerals inherent in the sludge-derived biochar for As(V) immobilization, Chem. Eng. J. 417 (2021) 129183.
[29] A. Francis, E. Ionescu, C. Fasel, R. Riedel, Crystallization Behavior and Controlling Mechanism of Iron-Containing Si–C–N Ceramics, Inorganic Chemistry 48(21) (2009) 10078-10083.
[30] J. Fan, X. Chen, Z. Xu, X. Xu, L. Zhao, H. Qiu, X. Cao, One-pot synthesis of nZVI-embedded biochar for remediation of two mining arsenic-contaminated soils: Arsenic immobilization associated with iron transformation, J. Hazard. Mater. 398 (2020) 122901.
[31] L. Ling, W. Zhang, Visualizing Arsenate Reactions and Encapsulation in a Single Zero-Valent Iron Nanoparticle, Environ. Sci. Technol. 51(4) (2017) 2288-2294.
[32] L. Ling, W. Zhang, Sequestration of Arsenate in Zero-Valent Iron Nanoparticles: Visualization of Intraparticle Reactions at Angstrom Resolution, Environ. Sci. Technol. Lett. 1(7) (2014) 305-309.
[33] W. Yan, R. Vasic, A.I. Frenkel, B.E. Koel, Intraparticle Reduction of Arsenite (As(III)) by Nanoscale Zerovalent Iron (nZVI) Investigated with In Situ X-ray Absorption Spectroscopy, Environ. Sci. Technol. 46(13) (2012) 7018-7026.
[34] S. Pang, J. Jiang, J. Ma, Oxidation of Sulfoxides and Arsenic(III) in Corrosion of Nanoscale Zero Valent Iron by Oxygen: Evidence against Ferryl Ions (Fe(IV)) as Active Intermediates in Fenton Reaction, Environ. Sci. Technol. 45(1) (2011) 307-312.

546 [35] C.M. McCann, C.L. Peacock, K.A. Hudson-Edwards, T. Shrimpton, N.D. Gray, K.L.
547 Johnson, In situ arsenic oxidation and sorption by a Fe-Mn binary oxide waste in soil, J.
548 Hazard. Mater. 342 (2018) 724-731.
549 [36] R. Gubler, L.K. ThomasArrigo, Ferrous iron enhances arsenic sorption and oxidation by
550 non-stoichiometric magnetite and maghemite, J. Hazard. Mater. 402 (2021) 123425.
551 [37] Y. Yoon, W.K. Park, T. Hwang, D.H. Yoon, W.S. Yang, J. Kang, Comparative
552 evaluation of magnetite–graphene oxide and magnetite-reduced graphene oxide
553 composite for As(III) and As(V) removal, J. Hazard. Mater. 304 (2016) 196-204.
554 [38] T.D. Sowers, J.M. Harrington, M.L. Polizzotto, O.W. Duckworth, Sorption of arsenic to
555 biogenic iron (oxyhydr)oxides produced in circumneutral environments, Geochim.
556 Cosmochim. Acta 198 (2017) 194-207.
557 [39] J. Luo, X. Li, C. Ge, K. Müller, H. Yu, P. Huang, J. Li, D.C.W. Tsang, N.S. Bolan, J.
558 Rinklebe, H. Wang, Sorption of norfloxacin, sulfamerazine and oxytetracycline by
559 KOH-modified biochar under single and ternary systems, Bioresource Technology 263
560 (2018) 385-392.
561 [40] V.T. Luong, E.E. Cañas Kurz, U. Hellriegel, T.L. Luu, J. Hoinkis, J. Bundschuh, Iron-
562 based subsurface arsenic removal technologies by aeration: A review of the current state
563 and future prospects, Water Res. 133 (2018) 110-122.
564 [41] G. Ona-Nguema, G. Morin, Y. Wang, A.L. Foster, F. Juillot, G. Calas, G.E. Brown,
565 XANES Evidence for Rapid Arsenic(III) Oxidation at Magnetite and Ferrihydrite
566 Surfaces by Dissolved O2 via Fe2+-Mediated Reactions, Environ. Sci. Technol. 44(14)
567 (2010) 5416-5422.
568 [42] Y. Yuan, N. Bolan, A. Prévoteau, M. Vithanage, J.K. Biswas, Y.S. Ok, H. Wang,
569 Applications of biochar in redox-mediated reactions, Bioresource Technology 246
570 (2017) 271-281.
571 [43] N.K. Niazi, I. Bibi, M. Shahid, Y.S. Ok, E.D. Burton, H. Wang, S.M. Shaheen, J.
572 Rinklebe, A. Lüttge, Arsenic removal by perilla leaf biochar in aqueous solutions and
573 groundwater: An integrated spectroscopic and microscopic examination, Environ.
574 Pollut. 232 (2018) 31-41.
575 [44] D. Zhong, Y. Jiang, Z. Zhao, L. Wang, J. Chen, S. Ren, Z. Liu, Y. Zhang, D.C.W.
576 Tsang, J.C. Crittenden, pH Dependence of Arsenic Oxidation by Rice-Husk-Derived
577 Biochar: Roles of Redox-Active Moieties, Environ. Sci. Technol. 53(15) (2019) 9034-
578 9044.
579 [45] D. Wang, D. Huang, S. Wu, G. Fang, F. Zhu, N. Chen, S. Liu, C. Zhu, D. Zhou,

580 Pyrogenic Carbon Initiated the Generation of Hydroxyl Radicals from the Oxidation of
581 Sulfide, Environ. Sci. Technol. (2021).
582 [46] S.S.A. Alkurdi, I. Herath, J. Bundschuh, R.A. Al-Juboori, M. Vithanage, D. Mohan,
583 Biochar versus bone char for a sustainable inorganic arsenic mitigation in water: What
584 needs to be done in future research?, Environment International 127 (2019) 52-69.
585 [47] F. Zhang, X. Wang, J. Xionghui, L. Ma, Efficient arsenate removal by magnetite-
586 modified water hyacinth biochar, Environ. Pollut. 216 (2016) 575-583.
587 [48] M. Keiluweit, P.S. Nico, M.G. Johnson, M. Kleber, Dynamic Molecular Structure of
588 Plant Biomass-Derived Black Carbon (Biochar), Environ. Sci. Technol. 44(4) (2010)
589 1247-1253.
590 [49] Y. Li, X. Qi, G. Li, H. Wang, Efficient removal of arsenic from copper smelting
591 wastewater via a synergy of steel-making slag and KMnO4, Journal of Cleaner
592 Production 287 (2021) 125578.
593 [50] E.J. Kim, K. Baek, Selective recovery of ferrous oxalate and removal of arsenic and
594 other metals from soil-washing wastewater using a reduction reaction, Journal of
595 Cleaner Production 221 (2019) 635-643.
596 [51] L. Tang, H. Feng, J. Tang, G. Zeng, Y. Deng, J. Wang, Y. Liu, Y. Zhou, Treatment of
597 arsenic in acid wastewater and river sediment by Fe@Fe2O3 nanobunches: The effect of
598 environmental conditions and reaction mechanism, Water Res. 117 (2017) 175-186.
599 [52] Y. Qiu, X. Xu, Z. Xu, J. Liang, Y. Yu, X. Cao, Contribution of different iron species in
600 the iron-biochar composites to sorption and degradation of two dyes with varying
601 properties, Chem. Eng. J. 389 (2020) 124471.
602 [53] Y. Zhang, X. Xu, P. Zhang, Z. Ling, H. Qiu, X. Cao, Pyrolysis-temperature depended
603 quinone and carbonyl groups as the electron accepting sites in barley grass derived
604 biochar, Chemosphere 232 (2019) 273-280.
605 [54] J. Shi, H. Han, C. Xu, A novel enhanced anaerobic biodegradation method using biochar
606 and Fe(OH)3@biochar for the removal of nitrogen heterocyclic compounds from coal
607 gasification wastewater, Sci. Total Environ. 697 (2019) 134052.
608 [55] S. Zhu, S.-H. Ho, X. Huang, D. Wang, F. Yang, L. Wang, C. Wang, X. Cao, F. Ma,
609 Magnetic Nanoscale Zerovalent Iron Assisted Biochar: Interfacial Chemical Behaviors
610 and Heavy Metals Remediation Performance, ACS Sustainable Chemistry &
611 Engineering 5(11) (2017) 9673-9682.
612 [56] X. Hu, Z. Ding, A.R. Zimmerman, S. Wang, B. Gao, Batch and column sorption of
613 arsenic onto iron-impregnated biochar synthesized through hydrolysis, Water Res. 68

614 (2015) 206-216.
615 [57] L. Kluepfel, M. Keiluweit, M. Kleber, M. Sander, Redox Properties of Plant Biomass-
616 Derived Black Carbon (Biochar), Environ. Sci. Technol. 48(10) (2014) 5601-5611.
617 [58] T. Zhang, Y. Zhao, S. Kang, H. Bai, W. Gu, D. Fang, S. Komarneni, Q. Zhang,
618 Mechanical activation of zero-valent iron (ZVI) in the presence of CaCO3: Improved
619 reactivity of ZVI for enhancing As(III) removal from water, Journal of Cleaner
620 Production 286 (2021) 124926.
621 [59] S.W. Poulton, D.E. Canfield, Development of a sequential extraction procedure for iron:
622 implications for iron partitioning in continentally derived particulates, Chemical
623 Geology 214(3) (2005) 209-221.
624 [60] S.P. Slotznick, J.M. Eiler, W.W. Fischer, The effects of metamorphism on iron
625 mineralogy and the iron speciation redox proxy, Geochim. Cosmochim. Acta 224 (2018)
626 96-115.
627 [61] L. Ling, X. Huang, M. Li, W.-x. Zhang, Mapping the Reactions in a Single Zero-Valent
628 Iron Nanoparticle, Environ. Sci. Technol. 51(24) (2017) 14293-14300.
629 [62] D. Zhong, Z. Zhao, Y. Jiang, X. Yang, L. Wang, J. Chen, C.-Y. Guan, Y. Zhang,
630 D.C.W. Tsang, J.C. Crittenden, Contrasting abiotic As(III) immobilization by
631 undissolved and dissolved fractions of biochar in Ca2+-rich groundwater under anoxic
632 conditions, Water Res. 183 (2020) 116106.
633 [63] H. Pan, X. Yang, H. Chen, B. Sarkar, N. Bolan, S.M. Shaheen, F. Wu, L. Che, Y. Ma, J.
634 Rinklebe, H. Wang, Pristine and iron-engineered animal- and plant-derived biochars
635 enhanced bacterial abundance and immobilized arsenic and lead in a contaminated soil,
636 Sci. Total Environ. 763 (2021) 144218.
637 [64] Z. Wen, J. Xi, J. Lu, Y. Zhang, G. Cheng, Y. Zhang, R. Chen, Porous biochar-supported
638 MnFe2O4 magnetic nanocomposite as an excellent adsorbent for simultaneous and
639 effective removal of organic/inorganic arsenic from water, J. Hazard. Mater. 411 (2021)
640 124909.
641 [65] H. Kim, J. Kim, T. Kim, D.S. Alessi, K. Baek, Mobility of arsenic in soil amended with
642 biochar derived from biomass with different lignin contents: Relationships between
643 lignin content and dissolved organic matter leaching, Chem. Eng. J. 393 (2020) 124687.
644 [66] Z. Xu, X. Xu, D.C.W. Tsang, F. Yang, L. Zhao, H. Qiu, X. Cao, Participation of soil
645 active components in the reduction of Cr(VI) by biochar: Differing effects of iron
646 mineral alone and its combination with organic acid, J. Hazard. Mater. 384 (2020)
647 121455.

[67] R. Daenzer, L. Xu, C. Doerfelt, Y. Jia, G.P. Demopoulos, Precipitation behaviour of As(V) during neutralization of acidic Fe(II)−As(V) solutions in batch and continuous modes, Hydrometallurgy 146 (2014) 40-47.

[68] K. Amstaetter, T. Borch, P. Larese-Casanova, A. Kappler, Redox Transformation of Arsenic by Fe(II)-Activated Goethite (α-FeOOH), Environ. Sci. Technol. 44(1) (2010) 102-108.

[69] H. Xu, Y. Sun, J. Li, F. Li, X. Guan, X., Aging of Zerovalent Iron in Synthetic Groundwater: X-ray Photoelectron Spectroscopy Depth Profiling Characterization and Depassivation with Uniform Magnetic Field. Environ. Sci. Technol. 50(15) (2016) 8214-8222.

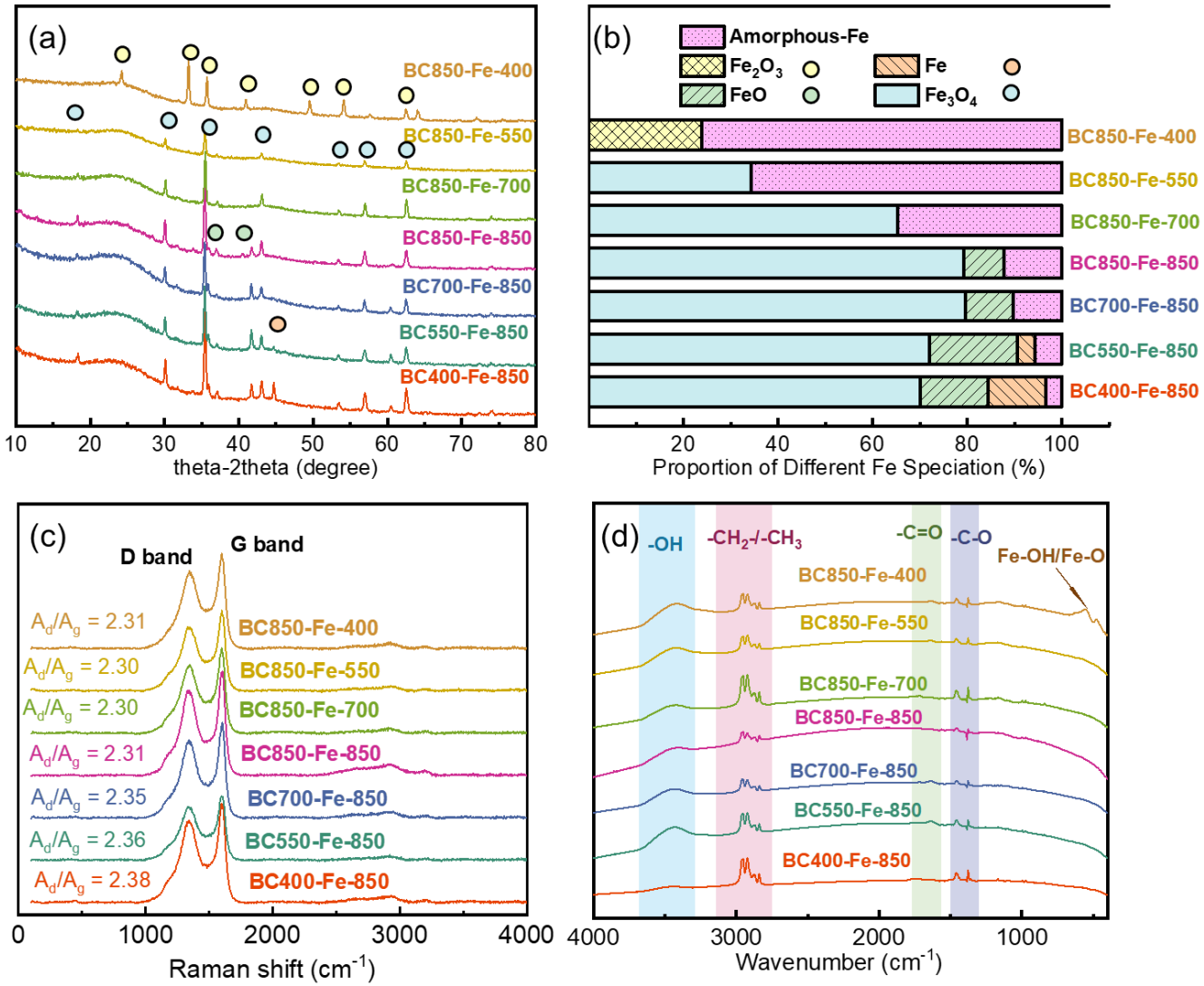

Figure 1. XRD patterns (a), semi-quantitative Q-XRD analysis (b), Raman spectra (c), and FTIR spectra (d) of different Fe-biochars (Hematite: Fe_2O_3; Magnetite: Fe_3O_4; Wustite: FeO; Metallic Fe: Fe).

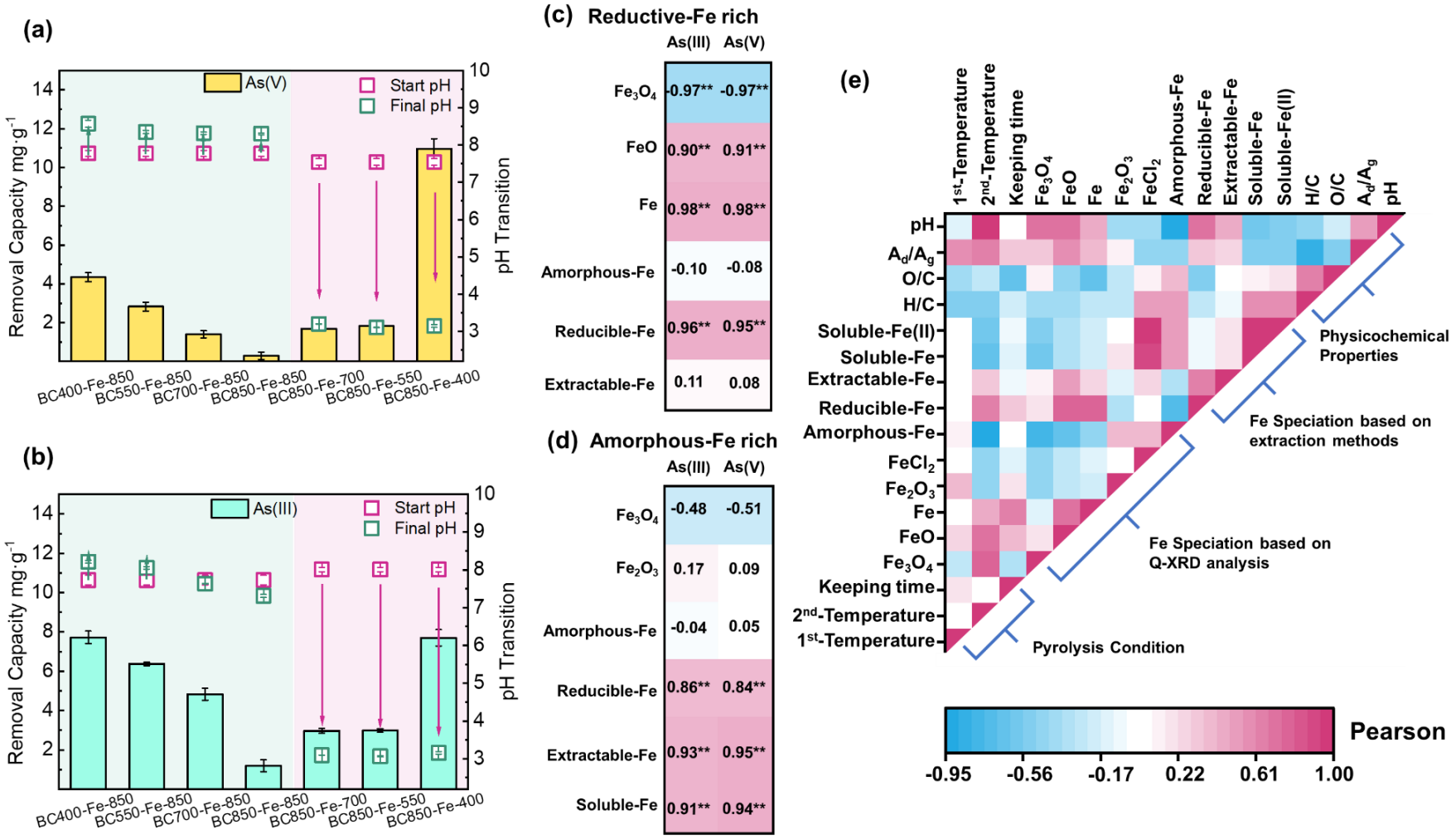

Figure 2. Removal capacities for As(V) (a) and As(III) (b) of the Fe-biochars and the change of solution pH after the reaction. Pearson correlation coefficient analysis of the As(III)/(V) removal capacities and Fe-speciation in the Fe-biochars containing abundant reductive-Fe (c) or abundant amorphous-Fe (d) (**p < 0.01, *p < 0.05). Pearson correlation matrix of the pyrolysis conditions, Fe speciation, and physicochemical properties of all Fe-biochars (e).

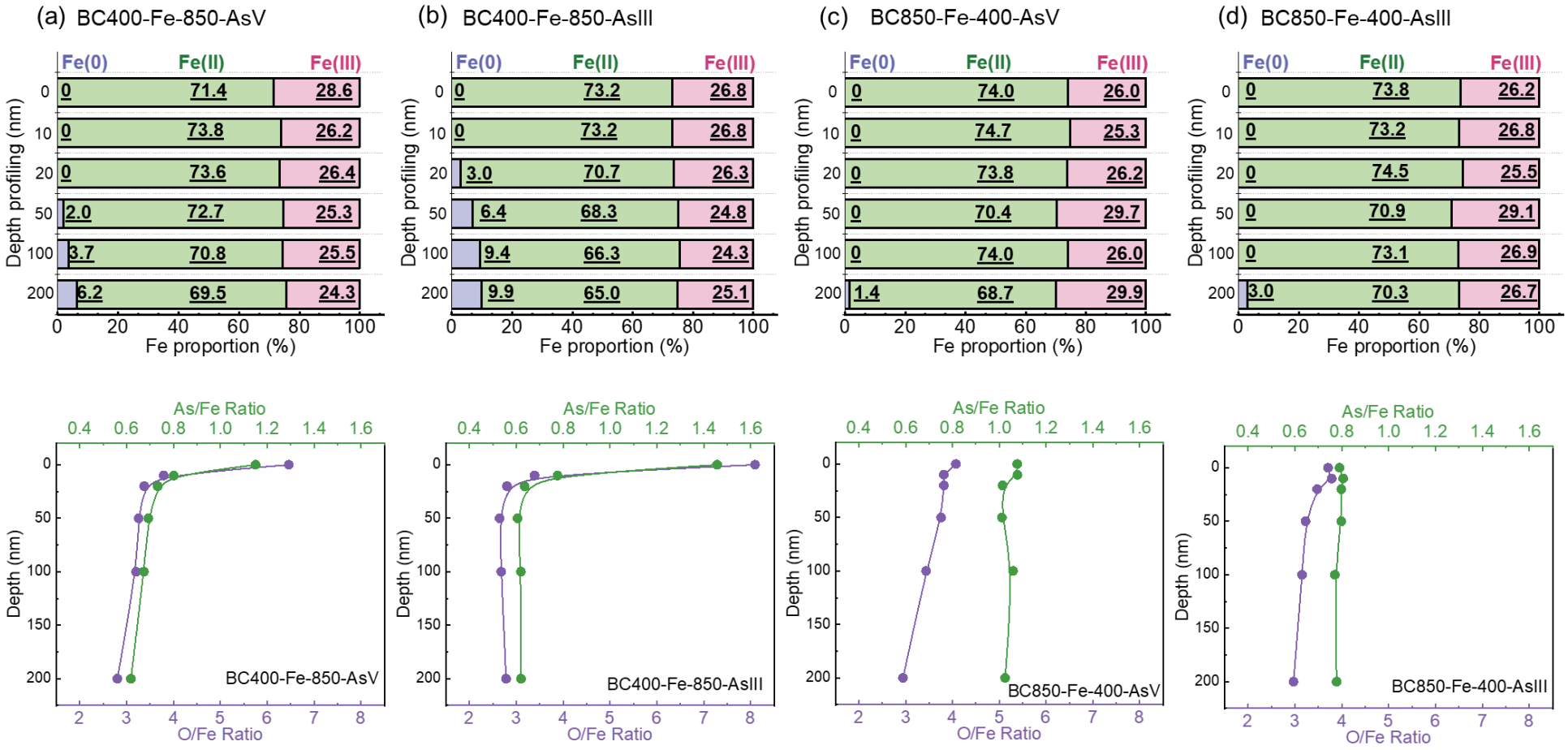

Figure 3. Depth-profiling XPS analysis of the Fe speciation (upper part) and atomic elemental ratio (O/Fe and As/Fe) (down part) on the typical Fe-biochars after As removal.

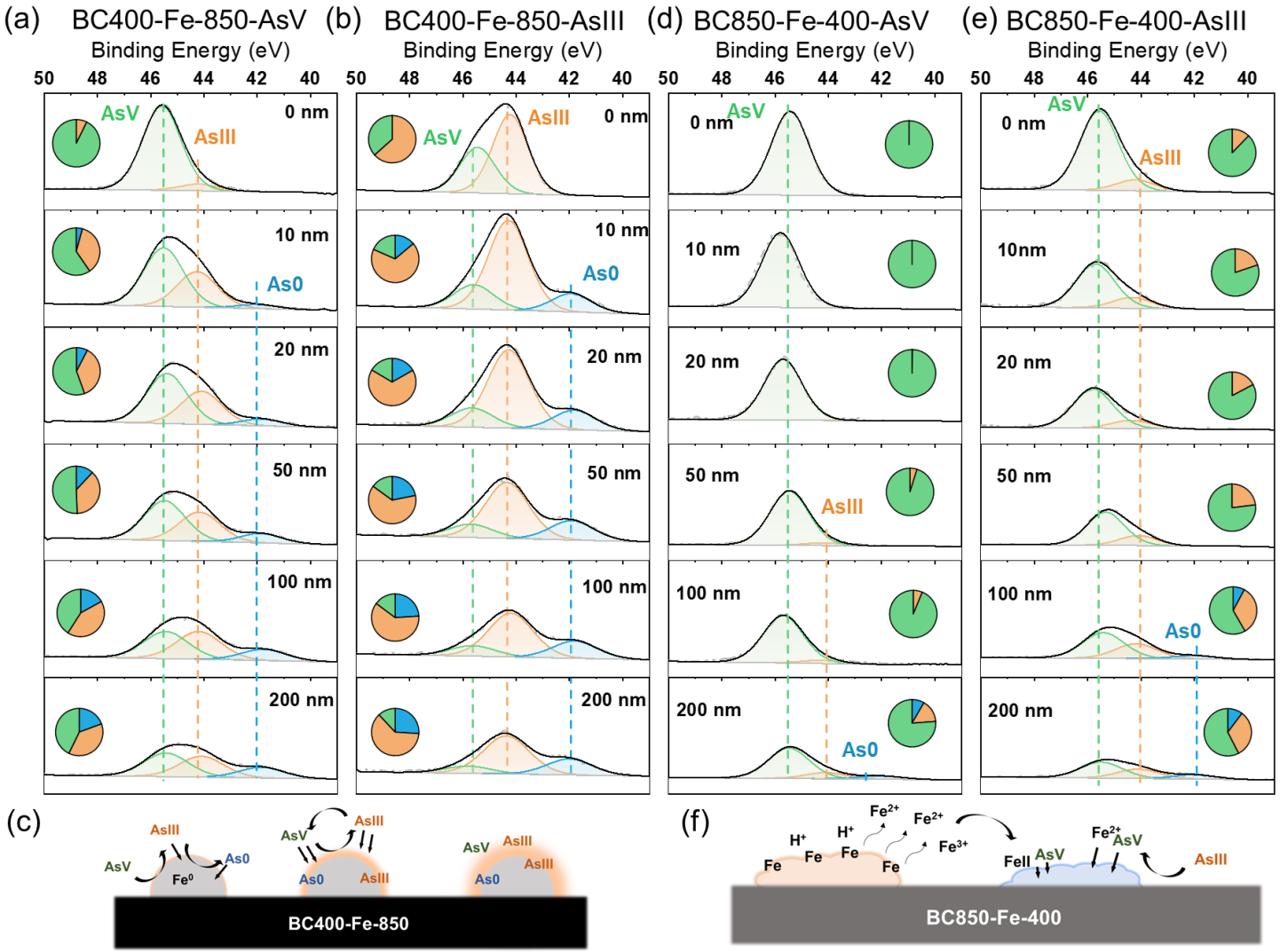

Figure 4. Depth-profiling XPS analysis of As 3d binding state on the typical Fe-biochars after As removal (a, b, d, e). The schematic diagram of As immobilization mechanisms by the Fe-biochars (c, f).